

# Observation of broadening Rashba-type band in Au<sub>2</sub>Sb surface alloy

Jinbang Hu<sup>1,†</sup>, Xiansi Wang<sup>2</sup>, Justin W Wells<sup>1,3,†</sup>

<sup>1</sup>*Department of Physics, NTNU, Trondheim, Norway.*

<sup>2</sup>*Hunan University, Changsha, 410082, China.*

<sup>3</sup>*Semiconductor Physics, Department of Physics, University of Oslo (UiO), NO-0371 Oslo, Norway*

<sup>†</sup>Corresponding author: jinbang.hu@ntnu.no; j.w.wells@fys.uio.no.

## Abstract

Here, we report a novel Au<sub>2</sub>Sb two-dimensional (2D) superstructure on Au(111) that shows agreements and discrepancies to the expected electronic features of the ideal 2D surface alloys with  $\sqrt{3} \times \sqrt{3}$  periodicity. Using spin- and angle-resolved photoemission spectroscopy, we find a significant spin splitting of the alloy bands with antiparallel spin polarization. The band structure originates from the hybridization between the Sb and the Au orbitals at the 2D Sb-Au interface. Taking advantage of the good agreement between the experimental results and DFT calculations, we find the broadening of the band is due to the perturbations introduced by the 3-pointed-star-shaped defects as nonresonant impurities in the  $8 \times 8$  superstructure. The periodic defect can properly adjust the energy position of the Rashba band while not breaking the in-plane symmetry.

## Introduction

Since the experiment discovery of 2D graphene, the investigation on 2D materials has attracted a lot of attentions<sup>1</sup>. Plenty of efforts are made to improve the tunability and performance of variety of 2D materials. The exfoliation of single layer black phosphorous opened a door to the investigation on VA-elements 2D materials, thanks to their excellent features<sup>2</sup>. Compared to mechanical exfoliation, molecular beam (MBE) epitaxial growth of 2D materials is more controllable and more flexible for different systems. Among VA elements, bismuthine has been successfully manufactured by MBE on SiC<sup>3</sup> and Ag<sup>4</sup>, which shows exotic topological features. During the growth of monoelemental 2D materials on metals (such as Cu, Ag, and Au), due to the strong interfacial interaction, the atoms of the sample material are adsorbed on the substrate, so that at low coverage a surface alloy is formed. The surface alloy may also possesses interesting properties<sup>5</sup>.

One of the reasons why the 2D materials are interesting is the presence of Rashba spin-orbit coupling (SOC) effect<sup>6</sup>, which exists in inversion-symmetry broken systems. Rashba SOC is related to rich physical phenomena and can break the degeneracy of spin degree of freedom without any external field or simultaneous magnetization, which is useful in spintronics applications. Materials of VA elements are also a versatile playground for the research on Rashba physics, such as Bi<sup>7</sup> and Sb<sup>8</sup>. In this paper, we introduce a Au<sub>2</sub>Sb surface alloy with the periodic defects decorated. The existence of the spin splitting of the alloy bands with antiparallel spin polarization are demonstrate by (spin) angle-resolved photoemission spectroscopy (ARPES). The good agreement between density functional theory (DFT) calculations and the experimental results confirms the periodic distributed structural defects

in Au<sub>2</sub>Sb surface alloy belongs to nonresonant impurities and the nearby crossing point of the Rashba bands can be shifted by properly introducing periodic distributed structural defects.

## Methods

All sample preparation steps and experiments were performed under ultrahigh vacuum conditions better than  $4 \times 10^{-10}$  mbar. The Au(111) surface was prepared by repeated sputtering and annealing cycles. The quality of the clean surface was confirmed by the existence of sharp diffraction spots observed in low energy electron diffraction (LEED) that correspond to the well-known Au-herringbone reconstruction and the intensity of the surface state, e.g. the Shockley state confirmed by our ARPES measurement (see Figure S1 in the Supplemental Material)<sup>24</sup>. The Au<sub>2</sub>Sb surface alloy was prepared by depositing submonolayer Sb (purity 99.9999%) on clean Au(111) at room temperature (RT), or annealing the Sb thin film on Au(111) to 400 C°, producing a  $\sqrt{3} \times \sqrt{3} R30^\circ$  structure. The success of the sample preparation was confirmed by LEED and X-ray photoemission spectroscopy (XPS) spectra of Au 4f and Sb 3d core levels. Band structure measurements were performed at  $T \approx 115$  K using an aberration-corrected, energy-filtered photoemission electron microscope (EF-PEEM) (NanoESCA III, Scienta Omicron GmbH) equipped with a focused helium discharge lamp primarily generating He I photons at  $h\nu = 21.22$  eV. Pass energy  $EP = 25$  eV and a 0.5 mm entrance slit to the energy filter was used, yielding nominal energy and momentum resolutions of  $\Delta E = 50$  meV and  $\Delta k = 0.02 \text{ \AA}^{-1}$ . Spin-resolved ARPES measurements were performed using a monolayer-Au-coated Ir(001) crystal as a spin filter<sup>11,12</sup>. The spin filter measured the projection of the spin along  $\pm k_y$ , which is in-plane and perpendicular to one of the  $\Gamma M$  direction ( $\pm k_x$ ) of Au(111) SBZ. The spin-polarisation  $P_y$  was calculated from the measurements using:

$$P_y = (I_y \uparrow - I_y \downarrow) / (S(I_y \uparrow + I_y \downarrow))$$

where  $I_y \uparrow$  and  $I_y \downarrow$  are the intensities of the energy surface when filtering spin along  $+k_y$  and  $-k_y$ , respectively<sup>13</sup>. A Sherman function  $S = 0.6$  was set, based on preliminary calibration measurements<sup>13,14</sup>.

The density functional theory (DFT) calculations were performed using the Vienna Ab initio Simulation Package (VASP)<sup>15</sup>. The interactions between the valence electrons and ion cores were described by the projector augmented wave method<sup>15,16</sup>. The electron exchange and correlation energy was treated by the generalized gradient approximation with the Perdew-Burke-Ernzerhof functional<sup>17,18</sup>. The kinetic energy cutoff of the plane-wave basis was set to 400 eV as default. We did not use the large  $8 \times 8$  supercell for the calculation of band structure because of the unacceptable large resource consumption. For the simplified models, 22 layers of Au atoms were included with the bottom 20 layers fixed as the bulk crystal structure while the top three layers were relaxed. One monolayer of Au<sub>2</sub>Sb atoms was adsorbed on top side of the Au slab. The vacuum layer is thicker than 15 Å applied to eliminate spurious interaction between two adjacent slabs. The first Brillouin zone was sampled with the  $\Gamma$ -centered  $15 \times 15 \times 1$  k points. The structures were optimized until the forces on the atoms were less than 20 meV Å<sup>-1</sup>. To take it into account to study the band structure influenced by periodic defects, we built a  $2 \times 2$  supercells from the primitive  $\sqrt{3} \times \sqrt{3}$

3R30° unit cell. In the supercell, the Sb atoms are gradually replaced by Au atom. Spin-orbit coupling has been included unless otherwise stated. The 8×8 superstructure with the bottom 3 layers fixed is applied for STM simulation using a the Tersoff-Hamann approach<sup>23</sup>.

## Results and Discussion

### 1-Structure characterization

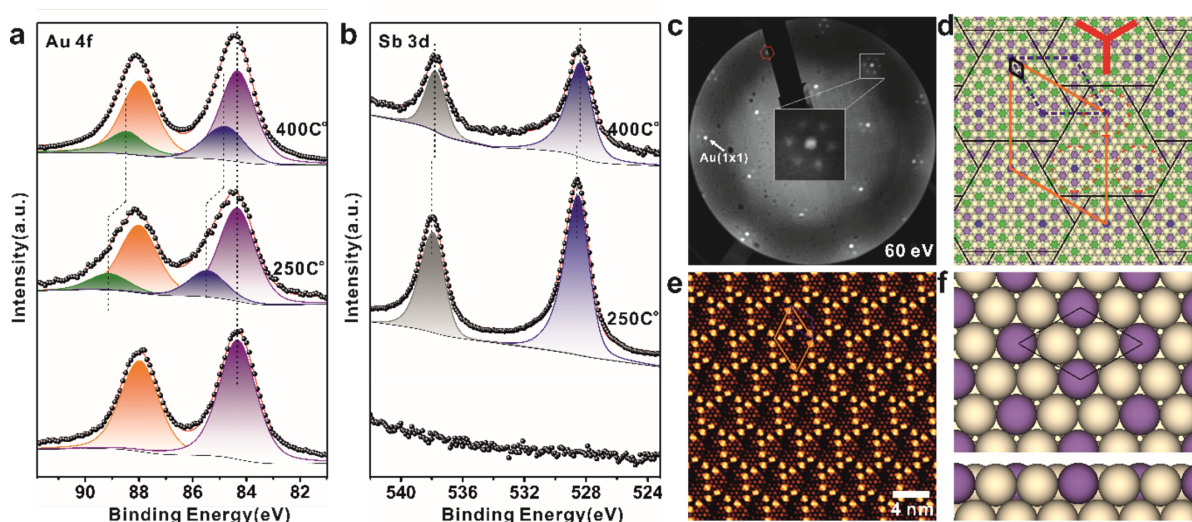


Figure 1. (a-b) XPS spectra of Au 4f (a) and Sb 3d (b) core levels taken for the Sb film after annealing at 250C° and further annealing at 400C°. (c) LEED pattern (60 eV) from  $\sqrt{3} \times \sqrt{3}R30^\circ$  Au<sub>2</sub>Sb surface alloy. The inset zooms in the diffraction around the Au(1x1) diffraction spot, presenting a 8×8 superstructure. (d) Energetically favourable atomic model and (e) STM simulation of surface alloy with 8×8 superstructure. The yellow rhombus and black dashed rhombus overlay in (d) to demonstrate the orientation and unit cell of 8×8 superstructure, respectively. The yellow balls are Au atoms, and balls of other colours are Sb atoms. A 3-pointed-star-shaped defect is marked by the thick red lines. (f) top and side view of fully optimized slab lattice of the Au<sub>2</sub>Sb surface alloy considered for band structure discussion.

Figure 1 presents the Au<sub>2</sub>Sb surface alloy fabricated on Au(111) at about 400 C°. XPS measurements were carried out to monitor the chemical shift of Au and Sb elements during the phase transition process, commencing from a well-prepared 2D  $3 \times \sqrt{3}$  structure followed by annealing up to 400 C°. Initial 2D Sb(110) rhombohedral phase on Au(111) surface could be prepared by annealing of a thicker Sb film sample, as reported in ref 1.<sup>9</sup>, and confirmed by the LEED pattern (60 eV) in Figure S2a. It is obvious in Figure 1a-b that the Sb 3d spectrum of as-fabricated 2D  $3 \times \sqrt{3}$  superstructure on the Au(111) surface at 250C° indeed has two components. These two characteristic signals, denoted as Sb 3d<sub>3/2</sub> and 3d<sub>5/2</sub>, appear at the lower binding energy side of Au 4p signal with energies 537.95 eV and 528.60 eV, respectively. Comparing to the Au 4f signal of clean Au(111), the peaks present a small systematic shift towards higher binding energy side by approximately 0.15 eV, and also deform in shape after the growth of the Sb monolayer. The fit of Au 4f signal reveals a remaining bulk component and a surface component at higher binding energy shifting towards the bulk component by 1.09 eV with respect to clean Au(111), mostly owing to the interaction with the Sb adlayer. Subsequently, annealing at 400°C was carried out, leading to changes in the shape of the Au 4f peak and a slight energy shift of 0.20 eV in the Sb 3d peaks towards the lower binding energy side. The fitting analysis of the Au 4f peak indicates that the surface component shifted by 0.50 eV towards the bulk component compared to clean Au(111). This observation suggests an Au-Sb surface alloy might be fabricated due to the

altered interaction between the Au surface and Sb adlayer. To further investigate the surface structure of Sb on Au(111) after annealing at 400°C, we obtained a LEED pattern (beam energy 60 eV) of a  $\sqrt{3} \times \sqrt{3}R30^\circ$  structure, as shown in Figure 1c. A clear moiré pattern surrounding the Au(1x1) diffraction spot is observed in the zoom-in LEED image when compared to that of the clean Au(111) surface. This observation signifies a phase transition from the monolayer  $3 \times \sqrt{3}$  rhombohedral phase to a  $8 \times 8$  superstructure. The formation of  $8 \times 8$  superstructure is in good agreement with the analysis based on atomically resolved STM images presented in References<sup>9</sup> and<sup>10</sup> (see Figure S4c, S5c in Ref.<sup>9</sup>, and Figure 3b in Ref.<sup>10</sup>).

To gain further insights into the experimental findings, we employed DFT calculations to construct an optimized  $8 \times 8$  structural model of the Au<sub>2</sub>Sb surface alloy, as depicted in Figure 1d. The 3-pointed-star-shaped defect is marked by thick red lines between the Sb (green) atoms. Subsequently, we conducted STM simulations based on this model decorated with Sb dimer, as shown in Figure 3e. Remarkably, the simulated STM image reproduces the features observed in previous experiments very well<sup>10</sup>. Notably, 12 equidistant dimers form a hexagon with three short sides and three long sides, originating from the adsorbed Sb dimers above the Au<sub>2</sub>Sb surface alloy. The Sb dimers act as an intermediate state of the alloying-to-dealloying transition as the Sb coverage increases to form a monolayer rhombohedral phase.

Additionally, we find that the same LEED pattern with moiré structure can be produced by directly depositing a submonolayer of Sb on the Au(111) surface, see Figure S2 in the Supplemental Material for details. The distinction lies in the Au<sub>2</sub>Sb alloy superstructure formed by depositing a submonolayer of Sb at room temperature (RT), which induces an aside small signal in XPS Sb 3d core level spectrum exhibiting a binding energy shift towards the higher side by 0.76 eV, corresponding to the Sb dimer assembly phase reported in Ref.<sup>10</sup>. However, the Au<sub>2</sub>Sb surface alloy fabricated by further annealing the dealloying  $3 \times \sqrt{3}$  rhombohedral phase demonstrates superior performance in achieving full alloying between Au and Sb, effectively avoiding various surface reconstructions.

## 2-Confirmation of band splitting

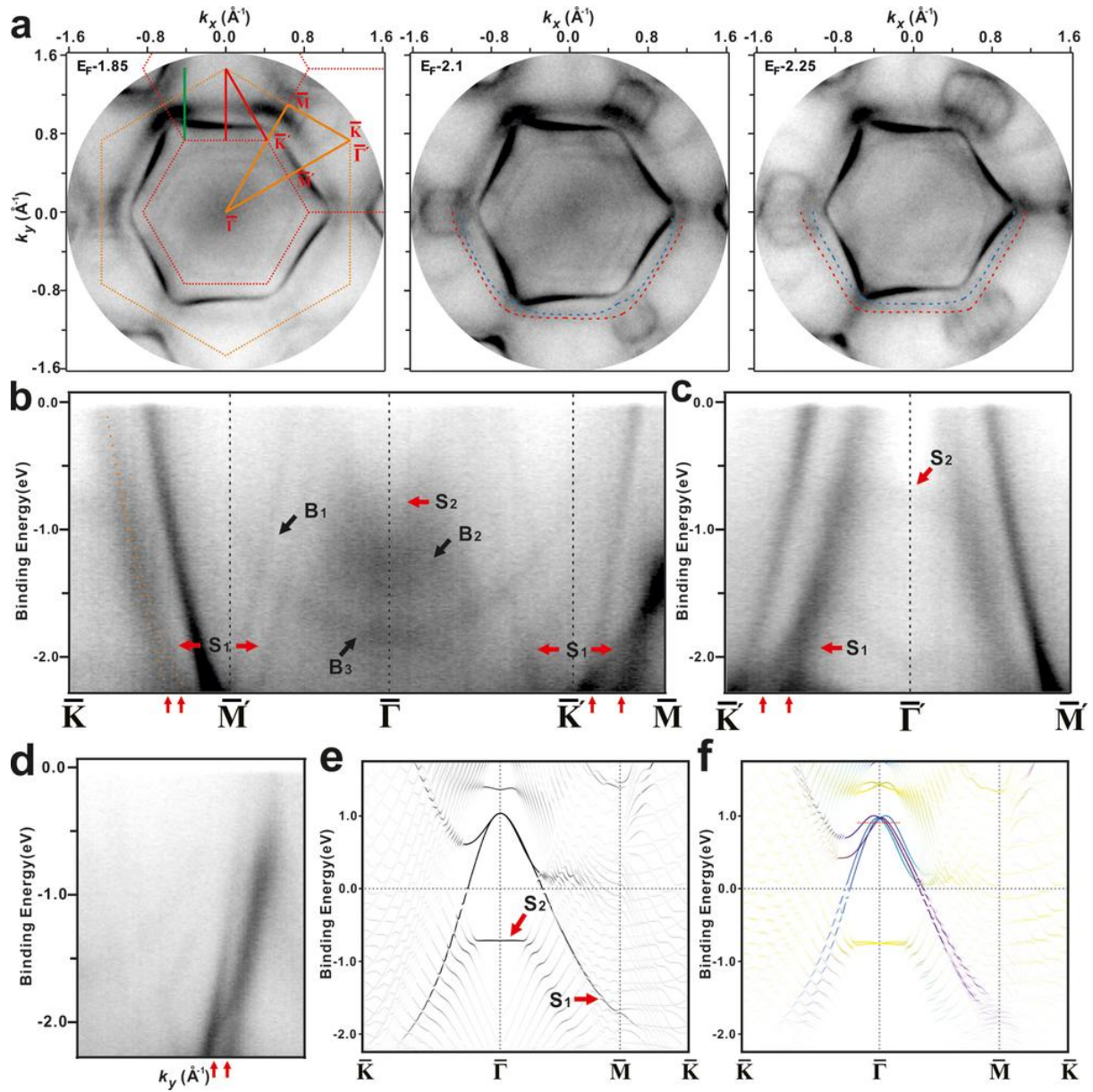


Figure 2. Electronic structure of Au<sub>2</sub>Sb surface alloy. (a) ARPES data of constant energy contours throughout the surface Brillouin zone at different binding energies.  $1 \times 1$  (yellow) and  $\sqrt{3} \times \sqrt{3}$  (red) surface Brillouin zone (SBZ) with symmetry point labels overlaid on the constant energy contours at 1.85 eV below the Fermi level. The red and blue dashed lines are used in (a) to guide the tendency of the splitting of the band. (b) and (c) ARPES results along high-symmetry directions of the Au(111) SBZ and the 2nd  $\sqrt{3} \times \sqrt{3}$  SBZ of the Au<sub>2</sub>Sb surface alloy. A few observations of particular interest are indicated by arrows. The dispersion feature  $B_1$  originates from umklapp scattered bulk Au sp band emission and  $B_{2,3}$  are replicas of the bulk band structure due to photoexcitation by the He I <sub>$\beta$</sub>  emission line of the nonmonochromatized He I light source, respectively. (d) energy-momentum slice along the green line marked in (a). (e-f) Calculated band structure without (e) and with (f) SOC for the model of the  $\sqrt{3} \times \sqrt{3}$  Au<sub>2</sub>Sb surface alloy in 1(f). Black symbols in (e) indicate contributions from the topmost Au<sub>2</sub>Sb layer. blue, pink, and yellow symbols indicate contributions from  $p_x$ ,  $p_y$ , and  $p_z$  states in (f). The red arrow at the bottom of (b-d) indicates the splitting character of  $S_1$ .

It would be intriguing to investigate the potential occurrence of Rashba splitting in Au<sub>2</sub>Sb surface alloy where the incorporated Sb atoms are surrounded by a similar ligand environment as widely observed in the  $\sqrt{3} \times \sqrt{3}R30^\circ$  structure. We now turn to the electronic band structure investigated by ARPES. Figure 2a-c represent the band structures of the Au<sub>2</sub>Sb surface alloy. The constant energy contours in Figure 2a exhibit features from both Au(111) and the Au<sub>2</sub>Sb surface alloy. Notably, a new captivating feature appears as a

distorted hexagon that connects the M point of the Au(111) SBZ. Upon closer inspection, the splitting of two sub-contours within the distorted hexagon band becomes larger with the binding energy increasing, as indicated by the red and blue dashed lines in Figure 2a. Interestingly, these shapes resemble those reported for Au<sub>2</sub>Sn<sup>19,21</sup>, as can be compared with Figures S2c-e in the Supplemental Material<sup>24</sup>.

In Figure 2a, the 1×1 (yellow) and  $\sqrt{3} \times \sqrt{3}$  (red) SBZs with high-symmetry point labels overlaid on the constant energy contours at 1.85 eV below the Fermi level is shown for the discussion of ARPES data. The band along the high symmetry path of Au(111) SBZ and the second  $\sqrt{3} \times \sqrt{3}$  SBZ are shown in Figure 2b and 2c. We observe the emergence of a new set of band features around the  $\Gamma$  point after Sb alloying on the Au surface. Specifically, the fuzzy S<sub>2</sub> band and hole-like parabolically dispersing bands S<sub>1</sub> and B<sub>1</sub> appear to be periodic with respect to the  $\sqrt{3} \times \sqrt{3}$  unit cell. The dispersion feature B<sub>1</sub> arises from umklapp scattering of Au sp band emission due to the presence of the  $\sqrt{3} \times \sqrt{3}$  structure. Additionally, weak bands B<sub>2</sub> and B<sub>3</sub> are observed in the first  $\sqrt{3} \times \sqrt{3}$  SBZ but are absent in the second  $\sqrt{3} \times \sqrt{3}$  SBZ. These bands represent replicas of the Au bulk band structure, resulting from photoexcitation by the He I $\beta$  emission line of the nonmonochromatized He I light source. Furthermore, all the bulk-related features observed in Figure 2b have also been observed on Sn/Au(111)- $\sqrt{3} \times \sqrt{3}$ <sup>19</sup>. The features we concern S<sub>1</sub> and S<sub>2</sub>, mixed with the Au bulk bands, look weak and fuzzy but exhibit higher signals in the second  $\sqrt{3} \times \sqrt{3}$  SBZ (Figure 2c). The splitting of two subbands in S<sub>1</sub> feature along the  $\Gamma$ K direction and also the slice (Figure 2d) along the green line marked in Figure 2a becomes clear as the binding energy increases. The spin degeneracy of S<sub>1</sub> is lifted even larger along K'M direction at a binding energy below -1.5 eV, see the left side in Fig. 2b. The evolution of splitting of band feature S<sub>1</sub> from Au<sub>2</sub>Sb surface alloy normal to  $\Gamma$ K direction is shown in Fig. S3a-b<sup>24</sup>. By the way, the emission intensity of S<sub>2</sub> is too weak to reveal any clear dispersive features.

To get better understanding on the band structure, DFT calculations with a well-ordered  $\sqrt{3} \times \sqrt{3}$  R30° lattice (Figure 1f) are performed. At this stage, compared to the 8×8 superstructure concluded from LEED and STM data<sup>10</sup>, the 3-pointed-star-shaped defects are ignored, since each Sb atom surrounded by a similar six Au ligands and in-plane symmetry (e.g six fold rotational symmetry and in-plane inversion symmetry) of 8×8 superstructure keeps the same as  $\sqrt{3} \times \sqrt{3}$  R30° lattice. Also, the 8×8 superstructure is too large for the numerical calculation. We start our discussion with the surface band structure without SOC and with SOC projected onto the topmost Au<sub>2</sub>Sb surface alloy layer along the  $\sqrt{3} \times \sqrt{3}$  SBZ, as shown in Figures 2e and 2f, respectively. The experimentally observed bands S<sub>1</sub> and S<sub>2</sub> can be identified. We can see that the inclusion of SOC induces obvious spin splitting of the bands. Bands S<sub>1</sub> display obvious separation of two spin subbands and steep dispersion. On the contrary, the calculated S<sub>2</sub> band located at a binding energy of 0.75 eV exhibits a flat region near the  $\Gamma$  point with quite weak splitting. The band structure calculated with SOC (Figure 2f) shows qualitative agreement with the experimentally observed bands S<sub>1</sub> and S<sub>2</sub>. Further analysis on the orbital-projected band structures of the d, p, and s orbitals (Figure 2f and S4) indicates that band S<sub>1</sub> mainly consists of Sb p<sub>//</sub> (p<sub>//</sub>=p<sub>x</sub>, p<sub>y</sub>) and Au d<sub>//</sub> (d<sub>//</sub>=d<sub>xy</sub>, d<sub>x<sup>2</sup>-y<sup>2</sup></sub>) orbitals, suggesting a direct hybridization between the Sb and Au

bands. On the other hand, the  $S_2$  hybrid band mainly contains Sb  $p_z$  and Au  $s$  orbital components.

### 3-Spin contrast and Rashba bands

One typical feature of Rashba SOC is the presence of helical spin texture of the band in  $k_x k_y$  plane. With Rashba SOC, the spin degeneracy is removed, resulting in two subbands with opposite spin directions. To further unravel the spin texture of the hole-like parabolic surface band  $S_1$ , we performed spin-resolved ARPES measurements. In-plane component (along  $k_y$  direction) of spin can be filtered. The spin filtering is realized by introducing a spin polarizing electron mirror into the electron optical path, where electrons with opposite spins experience different scattering potentials during the reflecting process<sup>11,20</sup>. Figure 3a-b show the individual spin resolved constant energy image at 2.13 eV below the Fermi level, and Figure 3c is the spin resolved image (see details about calculation of the spin resolved data in the Method section). It is found that the rarely spin polarized Au  $sp$  band is well removed, while two branches of Rashba-type  $S_1$  band show subtle sign of spin contrast. Figures 3d-f and 3g-i depict the band dispersion of the Rashba-type  $S_1$  state along the green line 1 and 2 marked in Figure 3c, respectively, where the line has nearly the same location as the slice in Figure 2e with a clear and strong splitting character of two subbands in  $S_1$  feature while the Au  $sp$  band with relatively weak intensity to make sure the  $S_1$  band rarely being blind by strong signal from Au  $sp$  band. As we can see in Figure 3d-f, it is apparent that the band dispersion dominated by spin-down ( $-k_y$ ) intensity in Figure 3d gives a smaller distance between Au  $sp$  band and  $S_1$  band than Figure 3e dominated by spin-up ( $+k_y$ ) intensity at a binding energy below  $-1.5$  eV. These features are more clearly demonstrated in spin resolved image (Figure 3e), and also the momentum distribution curves (MDCs) of spin polarization at binding energies of 1.9 eV (top panel of Figure 3(j)). Notably, the intensity profiles of the two subbands, marked by the green circle and black circle, respectively, appear to be opposite. Moreover, Figure 3g-i presents the analysis of the spin-resolved band dispersion along the green line 2 marked in Figure 3c, also revealing a spin-reversed result with the two branches of the  $S_1$  band. A representative DFT calculated spin texture of the rashba-type  $S_1$  band in  $k_x k_y$  plane at 0.9 eV above the Fermi level is shown in Figure 3k, where the arrows show the in-plane orientation of spin. Clear Rashba-type helical spin texture can be seen in the two branches of the  $S_1$  band with opposite spin polarization, which is in good agreement with our observation of spin-resolved ARPES measurements.

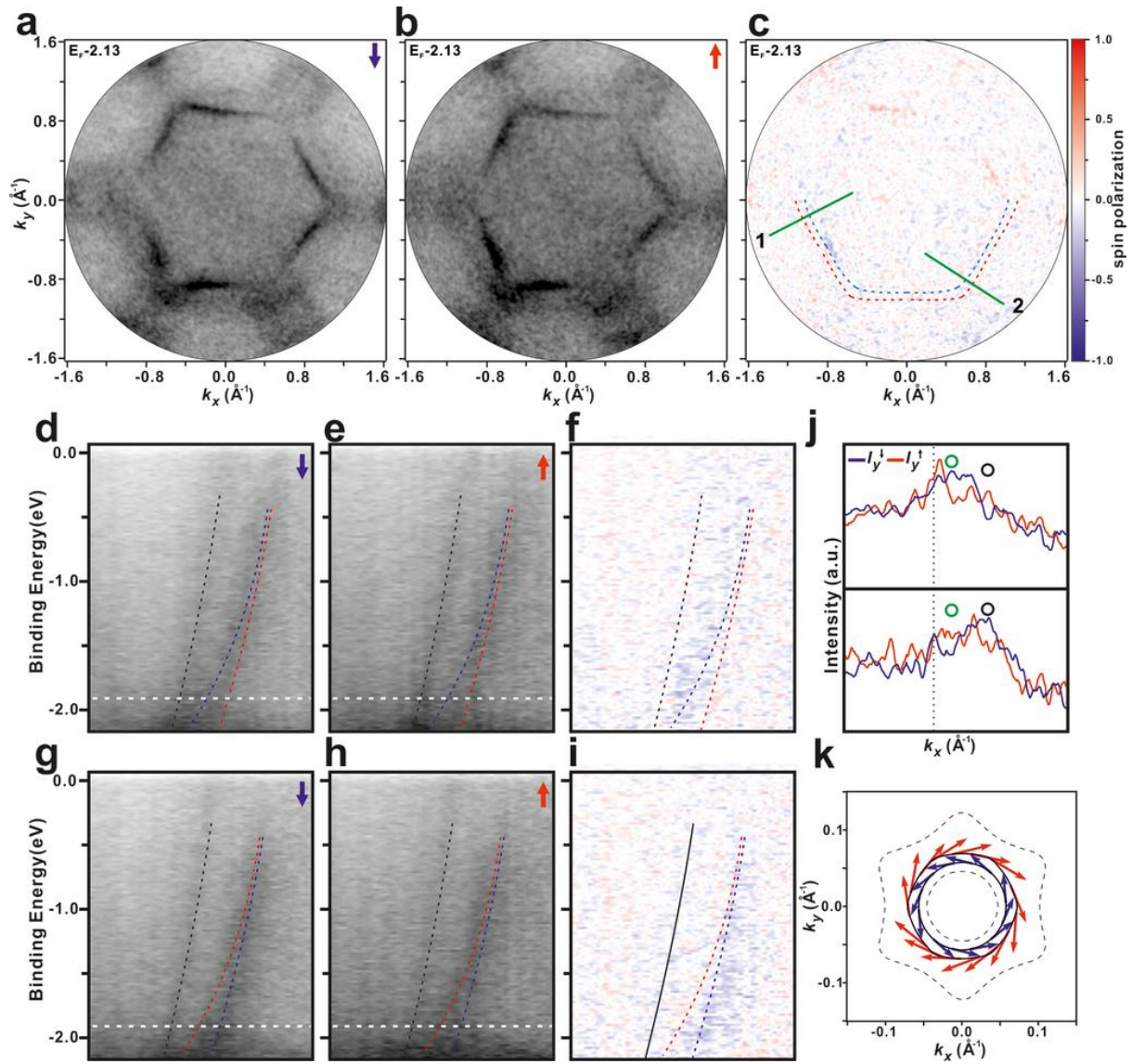


Figure 3. The  $k_y$ -oriented spin-resolved photoelectron momentum mapping of the Rashba-type band  $S_1$  measured by Au-coated Ir(100) as a spin filter at the working points at 10.95 eV (spin-down) and 12.30 eV (spin-up), respectively. (a-c) the constant energy image at 2.13 eV below the Fermi level, (a) the spin-down component, (b) the spin-up component (c) Spin resolved image. The colour scale indicates the spin polarization  $p_y$ , from  $p_y = -1$  (blue) to  $p_y = 1$  (red). (d-f) and (g-i) are the same as (a-c) but for band dispersion of the Rashba-type  $S_1$  states along the green line 1 and 2 marked in (c), respectively. The dark line, blue line and red line used in (d-i) as a reference of the position of Au sp band and two subbands of  $S_1$ . (j) In-plane spin polarized MDCs along  $k_x$  for energy marked as dashed line in (d-e) and (g-i), respectively. Red (blue) curves show the spin-up (spin-down) component of the intensity. The black dashed line and circle markers denote the peak positions of Au sp band and two subbands of  $S_1$  in the MDCs. (k) calculated spin texture of the Rashba-type  $S_1$  band in  $k_x$ - $k_y$  plane at  $E = E_F + 0.9$  eV marked by the red dashed white line in 2(f). The length and the direction of the arrows indicate the spin magnitude and direction.

The Rashba-type spin splitting band has been widely reported in similar systems such as  $\text{Au}_2\text{Sn}$  surface alloy<sup>9, 19</sup>. However, the pronounced Rashba-type band feature predicted by theoretical calculations in the  $\text{Au}_2\text{Sb}$  surface alloy appears to be less obvious in our experimental results. This discrepancy may be attributed to the ignored periodic defects, leading the coordinated Sb atom to perceive similar Au atoms as ligands with minimal discrepancy from the second-nearest Sb neighbour or Au in the branched Y-shaped defect. To gain further insight into the origin of the broadening character observed in the band

feature  $S_1$  from the  $\text{Au}_2\text{Sb}$  surface alloy, we introduced perturbations to the  $\text{Au}_2\text{Sb}$  surface alloy by subsequently substituting the Sb with an Au atom as a point defect in a  $2 \times 2$  reconstruction model for theoretical study (Figure 4).

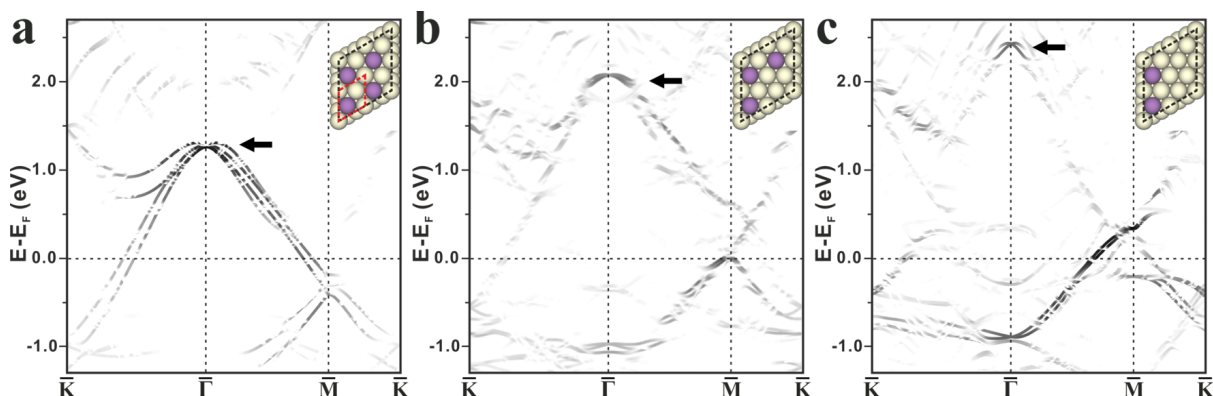


Fig. 4 Orbital decomposed band structure of  $\text{Au}_2\text{Sb}$  surface alloy with Sb defect, the structural defects introduced by subsequently substituting the Sb as Au atom. The black indicates the  $p_x + p_y$  orbital contributions of Sb in surface alloy. The  $2 \times 2$  slab models are shown at the bottom left of the corresponding calculation result. (a) perfect  $\text{Au}_8\text{Sb}_4$ , (b)  $\text{Au}_9\text{Sb}_3$ , (c)  $\text{Au}_{10}\text{Sb}_2$ . The crossing points of the Rashba band at  $\Gamma$  is marked by black arrow.

The band structure of the perfect  $2 \times 2$  model of the  $\text{Au}_2\text{Sb}$  surface alloy is plotted in Figure 4a, showing a clear Rashba-type band splitting as discussed earlier. However, when gradually substituting the Sb atoms in the  $2 \times 2$  supercell with Au atoms one by one to artificially create a “defective” structure, the two well-separated subbands gradually undergo an energy dependent broadening of the linewidth apart from the nearby crossing points of the Rashba band. This behaviour is typical for non-resonant impurities<sup>21</sup>. The components of Sb and Au within the  $8 \times 8$  superstructure can be written as  $\text{Au}_{135}\text{Sb}_{57}$ , in which the ratio of Sb is slightly lower than that of the perfect  $\text{Au}_2\text{Sb}$  surface alloy model but higher than the  $\text{Au}_9\text{Sb}_3$  defective model considered in figure 4b. Based on these observations, we deduce that the  $S_1$  band appears to be blurry but still possesses the Rashba splitting, which is consistent with our experimental observations.

## Summary

In conclusion, the atomic and electronic structures of the  $\text{Au}_2\text{Sb}$  surface alloys under different growing condition were prepared and studied involving LEED, XPS, (spin-)ARPES, and DFT calculations. From the LEED, STM simulation and the qualitative agreement between ARPES data and calculated band structure, we find that the Sb atoms can form an  $\text{Au}_2\text{Sb}$  surface alloy decorated by periodic defects. Apart from surface alloy deviates from the ideal  $\sqrt{3} \times \sqrt{3}R30^\circ$  periodicity, our ARPES measurement reveals a hole-like Rashba-type band feature  $S_1$  with remarkable broadening character in two splitting subbands, and the well agreement between spin-ARPES results and theoretically calculated spin texture of the  $S_1$  band confirms the helical spin texture of the band. An alternative explanation based on the periodic defects playing a role of nonresonant impurities has been proposed and confirmed by our theoretically study of  $\text{Au}_2\text{Sb}$  surface alloy by introducing defects(impurities) as perturbations, since the in-plane inversion symmetry and rotational symmetry of periodic impurities has been well kept. Moreover, Our calculation reveals that the nearby crossing point of the Rashba bands can be shifted by properly introducing

periodic distributed structural impurities with a similar in-plane symmetry as the surface alloy.

### **Acknowledgment**

This work was partially supported by the Research Council of Norway through its Centres of Excellence funding scheme, Project No. 262633, "QuSpin". X. S. W. acknowledges support from the Natural Science Foundation of China (NSFC) Grant No. 12174093 and the Fundamental Research Funds for the Central Universities.

## Reference

- 1 Mannix, A. J., Kiraly, B., Hersam, M. C. & Guisinger, N. P. Synthesis and chemistry of elemental 2D materials. *Nature Reviews Chemistry* **1**, 0014 (2017).
- 2 Xia, F., Wang, H. & Jia, Y. Rediscovering black phosphorus as an anisotropic layered material for optoelectronics and electronics. *Nature Communications* **5**, 4458 (2014).
- 3 Reis, F. *et al.* Bismuthene on a SiC substrate: A candidate for a high-temperature quantum spin Hall material. *Science* **357**, 287 (2017).
- 4 Sun, S. *et al.* Epitaxial growth of ultraflat bismuthene with large topological band inversion enabled by substrate-orbital-filtering effect. *ACS nano* **16**, 1436 (2021).
- 5 Wang, T., Park, M., Yu, Q., Zhang, J. & Yang, Y. Stability and synthesis of 2D metals and alloys: a review. *Materials Today Advances* **8**, 100092 (2020).
- 6 Rashba, E. Properties of semiconductors with an extremum loop. I. Cyclotron and combinational resonance in a magnetic field perpendicular to the plane of the loop. *Soviet physics-Solid state* **2**, 1109 (1960).
- 7 Mathias, S. *et al.* Quantum-well-induced giant spin-orbit splitting. *Physical Review Letters* **104**, 066802 (2010).
- 8 Sugawara, K. *et al.* Fermi surface and anisotropic spin-orbit coupling of Sb (111) studied by angle-resolved photoemission spectroscopy. *Physical Review Letters* **96**, 046411 (2006).
- 9 Cantero, E. D. *et al.* Synthesis and characterization of a pure 2d antimony film on au (111). *The Journal of Physical Chemistry C* **125**, 9273 (2021).
- 10 Zhou, D. *et al.* Interfacial effects on the growth of atomically thin film: Group VA elements on Au (111). *Advanced Materials Interfaces* **6**, 1901050 (2019).
- 11 Tusche, C., Krasnyuk, A. & Kirschner, J. Spin resolved bandstructure imaging with a high resolution momentum microscope. *Ultramicroscopy* **159**, 520 (2015).
- 12 Kirschner, J., Giebels, F., Gollisch, H. & Feder, R. Spin-polarized electron scattering from pseudomorphic Au on Ir (001). *Physical Review B* **88**, 125419 (2013).
- 13 Meier, F., Dil, J. H. & Osterwalder, J. Measuring spin polarization vectors in angle-resolved photoemission spectroscopy. *New Journal of Physics* **11**, 125008 (2009).
- 14 Sherman, N. Coulomb scattering of relativistic electrons by point nuclei. *Physical Review* **103**, 1601 (1956).
- 15 Kresse, G. & Joubert, D. From ultrasoft pseudopotentials to the projector augmented-wave method. *Physical Review B* **59**, 1758 (1999).
- 16 Blöchl, P. E. Projector augmented-wave method. *Physical Review B* **50**, 17953 (1994).
- 17 Perdew, J. P., Burke, K. & Ernzerhof, M. Generalized gradient approximation made simple. *Physical Review Letters* **77**, 3865 (1996).
- 18 Perdew, J. P., Burke, K. & Ernzerhof, M. Generalized Gradient Approximation Made Simple [Phys. Rev. Lett. 77, 3865 (1996)]. *Physical Review Letters* **78**, 1396 (1997).
- 19 Maniraj, M. *et al.* Structure and electronic properties of the (3×3) R 30° SnAu<sub>2</sub>/Au (111) surface alloy. *Physical Review B* **98**, 205419 (2018).
- 20 Kirschner, J. & Feder, R. Spin polarization in double diffraction of low-energy electrons from W (001): experiment and theory. *Physical Review Letters* **42**, 1008 (1979).

- 21 Kot, P. *et al.* Band dispersion of graphene with structural defects. *Physical Review B* **101**, 235116 (2020).
- 22 Shah, J. *et al.* Atomic and electronic structures of the Au<sub>2</sub>Sn surface alloy on Au(111). *Physical Review B* **104**, 125408 (2021).
- 23 Tersoff, J.; Hamann, D. R. Theory of the scanning tunneling microscope. *Phys Rev B Condens Matter* 1985, 31 (2), 805-813.
- 24 See Supplemental Material.

# Supplemental Material

## Observation of broadening Rashba-type band in AuSb surface alloy

Jinbang Hu<sup>1,†</sup>, Xiansi Wang<sup>2</sup>, Justin W Wells<sup>1,3,†</sup>

<sup>1</sup>*Department of Physics, NTNU, Trondheim, Norway.*

<sup>2</sup>*Hunan University, Changsha, 410082, China.*

<sup>3</sup>*Semiconductor Physics, Department of Physics, University of Oslo (UiO), NO-0371 Oslo, Norway*

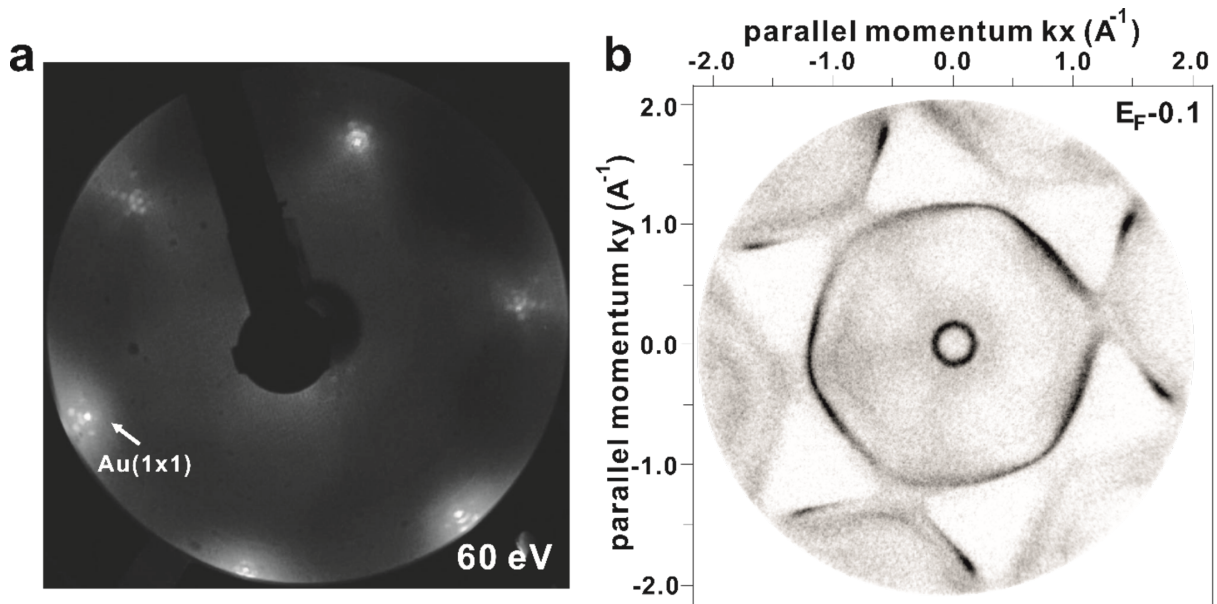


Fig. S1 (a) LEED pattern(60eV) of the clean Au(111) substrate. (b) ARPES data of constant energy contours throughout the surface Brillouin zone at 0.1eV below the Fermi level.

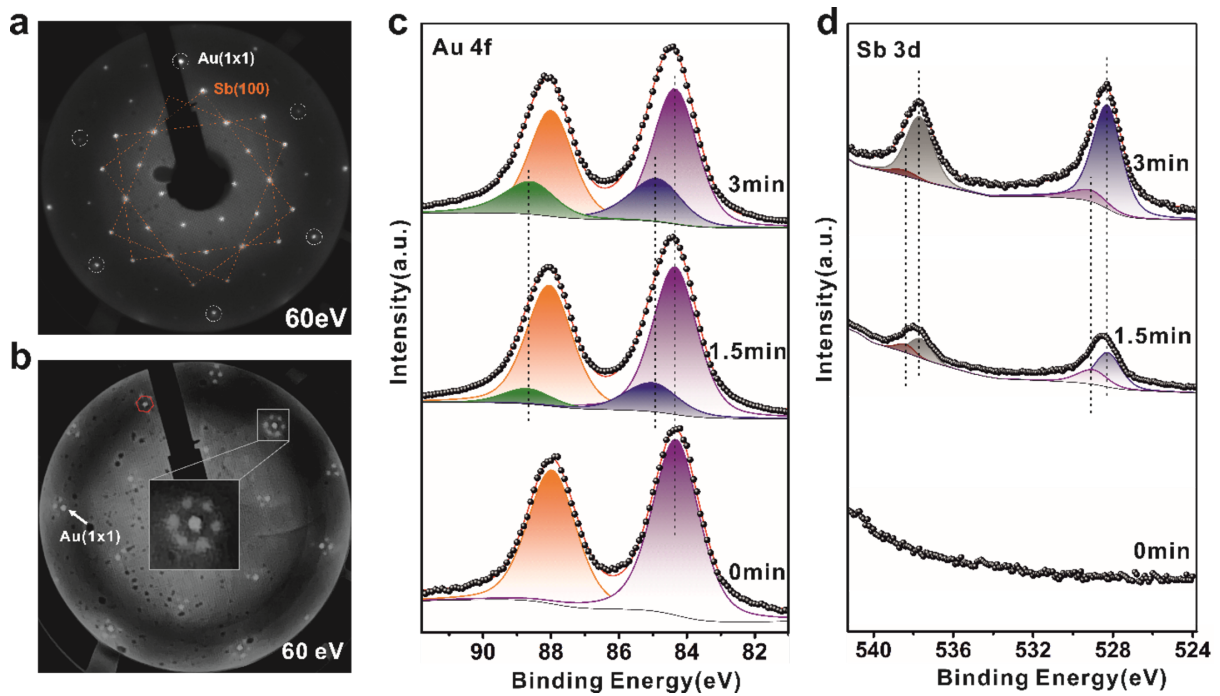


Fig. S2 (a) LEED pattern(60eV) of Sb monolayer grown on the Au(111) substrate. The unit cell of 2D Sb is proposed and highlighted by yellow dashed lines. (b) LEED pattern (60eV) from  $\sqrt{3} \times \sqrt{3}R30^\circ$  Au<sub>2</sub>Sb surface alloy formed after 3min Sb deposition at room temperature. The inset shows details of the diffraction around the Au(1x1) diffraction spot, presenting a 8x8 superstructure. (c-d) Evolution of Au 4f and Sb 3d core level as a function of Sb coverage at RT.

In Figure S2c-d, the Au 4f and Sb 3d core levels are presented to monitor the deposition of Sb onto the Au(111) substrate, leading from the clean surface to the formation of the  $\sqrt{3} \times \sqrt{3} R30^\circ$  Au<sub>2</sub>Sb surface alloy at room temperature. XPS spectrum shows Sb 3d signal after 1.5 min Sb deposition at RT. Simultaneously, the Au 4f core level exhibits alterations in both shape and energy. Our peak fitting of Sb 3d signal indicates there are two components in Sb 3d<sub>3/2</sub> signal and in 3d<sub>5/2</sub> signal, respectively, which the components at the higher binding energy side might attribute to Sb dimer formed on Au(111) at a low coverage, corresponding to the STM observation in Ref 1<sup>1</sup>. The components appearing at the lower binding energies of 537.95 and 528.60 eV agrees well with the Au-Sb alloy signal, as discussed in main text. Meanwhile, our fitting of Au 4f core level also indicates a higher binding energy component, which might come from the interaction between Au atom and Sb atom as surface alloy. Further deposition Sb on Au surface leads to a stronger Sb 3d signal with obvious component from surface alloy while the shoulder at higher binding energy become smaller, due to the surface phase transition from Sb dimer to Au<sub>2</sub>Sb surface alloy, and the fitting of Au 4f signal gives a consistently stronger surface component at the higher binding energy side shifted by 0.5 eV. Our LEED pattern in Fig. S1b shows a  $8 \times 8$  superstructure of Au<sub>2</sub>Sb surface alloy, which is quite similar to the  $8 \times 8$  superstructure formed by 2D Sb(110) rhombohedral phase on Au(111) surface annealing to 400 C°, discussed in the main text.

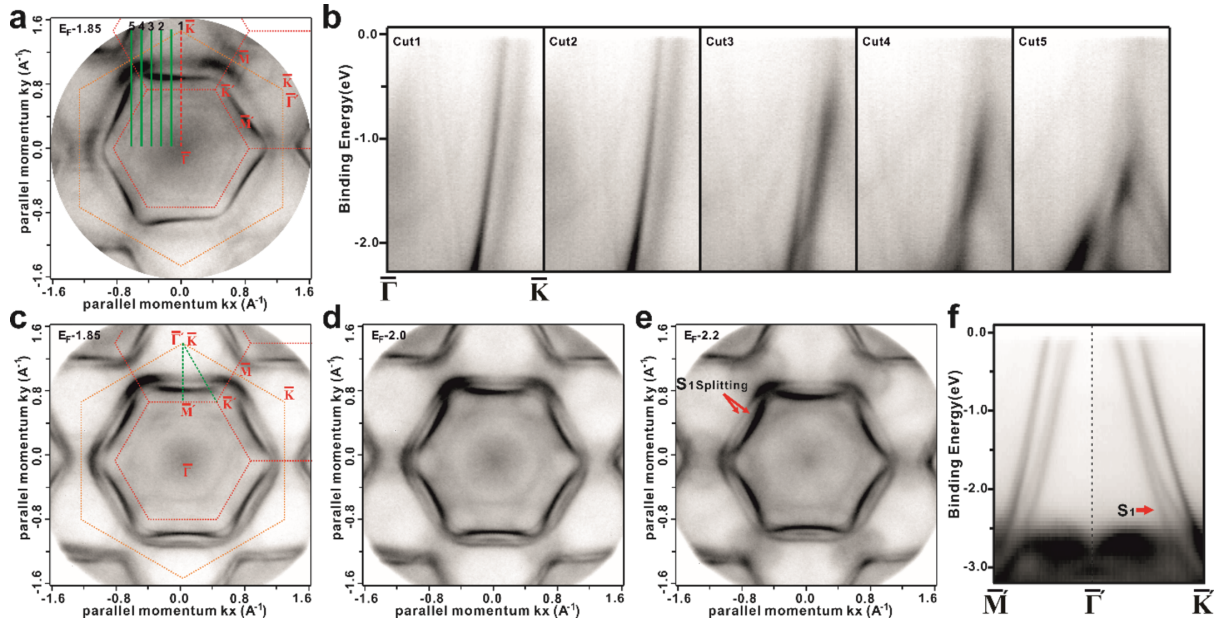


Fig. S3 (a) ARPES data of constant energy contours throughout the surface Brillouin zone at 1.85eV below the Fermi level. (b) band dispersion along the line marked as 1-5 in (a) to show the evolution of splitting of band feature  $S_1$ . ARPES data of constant energy contours (c-e) and band dispersion along high-symmetry directions of the 2nd  $3 \times 3$  SBZ of the  $Au_2Sn$  surface alloy as a reference to show the clear splitting of Rashba-type band feature  $S_1$ .

Fig.S3(a-b) show the evolution of splitting of band feature  $S_1$  from  $Au_2Sb$  surface alloy normal to  $\Gamma K$  direction. We can clearly find the splitting of the band feature  $S_1$  in cut2-5 even it's broadening in band dispersion. In Fig.S3c-f we show the electronic structure of  $Au_2Sn$  surface alloy as a reference. The sample preparation of  $Au_2Sn$  surface alloy followed the record in Ref. 2<sup>2</sup>. We found the two splitting branches of band feature  $S_1$  are sharp and well separated.

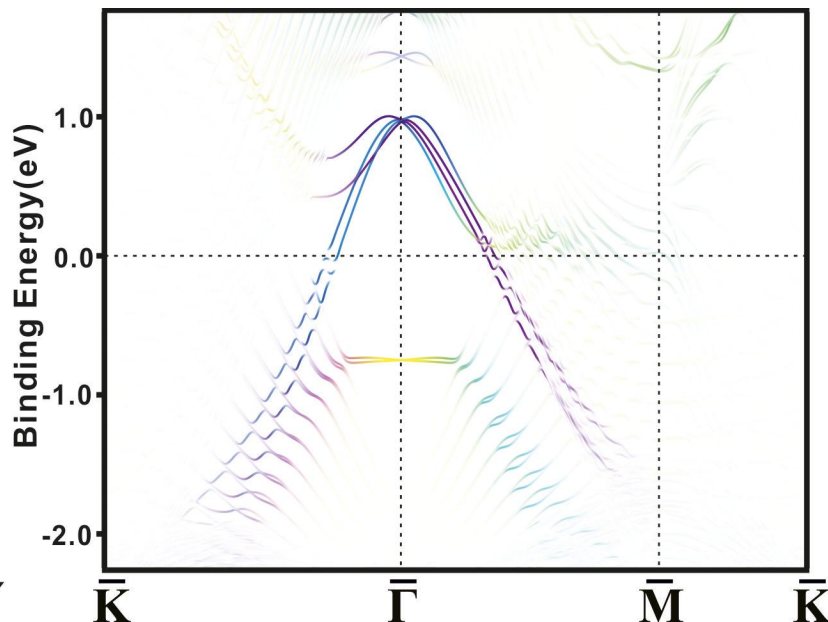


Fig. S4 Calculated band structure with SOC for the model of the  $\sqrt{3} \times \sqrt{3}$   $Au_2Sb$  surface alloy in 1(f). Blue, pink, and yellow symbols indicate contributions from  $d_{xy}$ ,  $d_{x^2-y^2}$ , and  $s$  states of the topmost  $Au_2Sb$  layer.

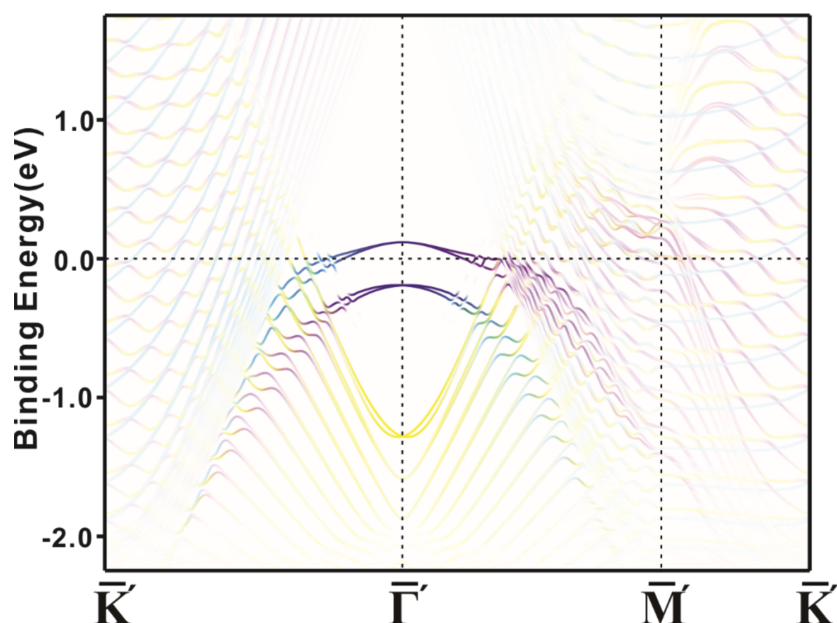


Fig. S4 Calculated band structure with SOC for the Sb adsorbed model with  $\sqrt{3} \times \sqrt{3}$  surface reconstruction. Blue, pink, and yellow symbols indicate contributions from px, py, and pz states projected from adsorbed Sb atom.

In Figure S4, the surface band projected from the adsorbed Sb atom exhibits a clear band dispersion around the gamma point, but its dispersion becomes less pronounced as the binding energy increases. This feature shows distinct differences with the calculated band structure from the Au<sub>2</sub>Sb alloy model and the experimental ARPES data.

## Reference

- 1 Zhou, D. *et al.* Interfacial effects on the growth of atomically thin film: Group VA elements on Au (111). *Advanced Materials Interfaces* **6**, 1901050 (2019).
- 2 Shah, J. *et al.* Atomic and electronic structures of the Au<sub>2</sub>Sn surface alloy on Au(111). *Physical Review B* **104**, 125408 (2021).